ADVANCING EARTH AND SPACE SCIENCES

JGR Atmospheres

RESEARCH ARTICLE
10.1029/2023JD039473

Key Points:

- Global warming intensifies the mesoscale convective system (MCS) during the record-breaking extreme rainfall event in July 2021 in Henan, China
- Global warming leads to a faster growth of MCS during its developing stage
- The interaction between terrains and moist flow may lead to different responses of rainfall centers to warming

Correspondence to:

J. Nie,
jinie@pku.edu.cn

Citation:

Lin, Z., Nie, J., Wang, J., Chen, Y., & Meng, Z. (2024). Responses of mesoscale convective system to global warming: A study on the Henan 2021 record-breaking rainfall event. *Journal of Geophysical Research: Atmospheres*, *129*, e2023JD039473. https://doi.org/10.1029/2023JD039473

Received 25 JUN 2023
Accepted 1 APR 2024

Responses of Mesoscale Convective System to Global Warming: A Study on the Henan 2021 Record-Breaking Rainfall Event

Zhongxi Lin[1,2], Ji Nie[1,2,3], Jun Wang[4], Yang Chen[5], and Zhiyong Meng[1,2]

[1]Department of Atmospheric and Oceanic Sciences, School of Physics, Peking University, Beijing, China, [2]China Meteorological Administration Tornado Key Laboratory, Foshan, China, [3]Institute of Carbon Neutrality, Peking University, Beijing, China, [4]The Key Laboratory of Land Surface Pattern and Simulation, Institute of Geographical Sciences and Natural Resources Research, Chinese Academy of Sciences, Beijing, China, [5]State Key Laboratory of Severe Weather, Chinese Academy of Meteorological Sciences, Beijing, China

Abstract The limited capabilities of global climate models in simulating mesoscale convective systems (MCSs) restrict our understanding of how global warming impacts MCSs. This study uses a high-resolution numerical model with large-ensemble experiments to simulate MCSs during the record-breaking extreme rainfall event in Henan Province, China, in July 2021. We compare the changes in the MCS's strength, size, and structure in a real-world simulation (RW) and a 0.8°C colder simulation (analog to no-anthropogenic-warming-world simulation, short for NAWW) to assess the response of MCSs to global warming. Our results show that the total rainfall from the MCS increased by 10.0% in RW compared to NAWW, with a 3.1% increase in area and a 6.7% increase in rainfall intensity. The development of MCS becomes more rapid in response to warming since the pre-industrial era. The warmer and wetter climate results in higher convective available potential energy, and accelerates the MCS growth, but then the narrower low-convective inhibition regions suppress the continuous growth of MCS. During the mature phase, the maximum hourly rainfall intensity (P_{max}) can increase by up to 26.5%/K, while P_{max} locations can either remain unchanged or shift depending on the interaction of flows and terrains. These results highlight varying responses of MCSs to global warming during its different stages and provide valuable insights into the changing characteristics of extreme rainfall events under global warming.

Plain Language Summary Mesoscale convective systems (MCSs) play a crucial role in generating heavy rainfall during severe rainfall events, such as the record-breaking rainfall occurred in Henan Province, China, in July 2021. Here, we investigate whether the MCSs during this extreme event are intensified due to global warming. We use a numerical model to simulate the MCSs under two different scenarios—the current climate background and a 0.8°C colder climate, which analog to the pre-industrial climate. Our results indicate that the total rainfall from MCSs increased by 10.0% due to global warming, with a 3.1% larger MCSs area and a 6.7% stronger hourly rainfall intensity. Global warming also leads to a faster development of MCSs by providing favorable warmer and wetter atmosphere. When the MCSs are mature, the maximum hourly rainfall intensity can increase by up to 26.5% per °C. The center of MCSs could remain unmoved or shift, depending on the interaction between low-level flow and terrain. This study illustrates that MCSs can produce much stronger rainfall under global warming with varying changes during the developing and mature phases. These results provide deeper insight into the impacts of global warming to extreme rainfall events.

1. Introduction

Mesoscale convective systems (MCSs) may produce extreme rainfall and result in disasters such as floods, hail, and landslides. In recent years, the potential responses of MCS and its associated extreme rainfall to global warming are becoming public-concern issues with the rise in global temperature and increasing reports of extreme weather (Feng et al., 2016; IPCC, 2021; Kendon et al., 2014; Ng et al., 2021; Prein et al., 2017; Westra et al., 2014). Westra et al. (2014) have found evidence of increasing intensities of short-duration extreme rainfall over many regions of the world. Several studies explored the response of MCS to global warming based on observations and model simulations (Dougherty et al., 2023; Feng et al., 2016; Fitzpatrick et al., 2020; Prein et al., 2017; Trapp et al., 2009). Observational studies also reported the frequency and intensity of MCSs increases

10.1029/2023JD039473

over America, west Africa, and the Amazon, but these trends are highly dependent on the regions and seasons (Feng et al., 2016; Fitzpatrick et al., 2020; Prein et al., 2017; Rehbein & Ambrizzi, 2023; Song et al., 2022).

The starting point for considering how global warming causes intensification in rainfall is that the atmosphere water vapor capacity increases accordingly to a Clausius-Clapeyron scale of 7%/K (CC rate). However, the short-duration rainfall response to warming can exceed the CC rate, leading to a super-CC rate (Lenderink et al., 2011; Trenberth et al., 2003; Westra et al., 2014). The super-CC rate is explained as a combined result of the increased proportion of convective rainfall, favorable dynamic condition, and cloud feedback (Haerter & Berg, 2009; Lenderink & van Meijgaard, 2009; Ng et al., 2021; Song et al., 2022; Westra et al., 2014). By producing more convective rainfall and enhancing the vertical motion, the intensification of MCSs also potentially contributes to the super-CC rate of short-duration extreme rainfall under global warming (Haerter & Berg, 2009). According to a modeling study (Prein et al., 2017), the responses of MCSs over North America to an approximately 4 K warming show that rainfall volume and intensity increase by the CC rate, and meanwhile the MCS areas broaden by up to 80%. The cloud top of MCSs rises by ∼2 km, expanding the convective system vertically and strengthening the vertical updraft. This and several other studies highlight the impact of global warming on MCS frequency and intensity by providing favorable warm and moist conditions and altering microphysics processes (Prein et al., 2017; Trapp & Hoogewind, 2016; Trapp et al., 2009). Some other studies also found that the changing large-scale circulation due to global warming plays a crucial role in increasing rainfall in MCSs (Fitzpatrick et al., 2020; Nie et al., 2018; Rehbein & Ambrizzi, 2023; Song et al., 2022; Trapp et al., 2009). While previous studies have generally treated MCSs as a whole system, it is worth considering the possibility that their responses to global warming may vary throughout their life cycles.

Between 19 and 21 July 2021, Henan Province in China experienced one of the heaviest rainfall events in regional and national history, resulting in widespread flooding across the province (J. Yin et al., 2022; Q. H. Zhang et al., 2023). The capital city, Zhengzhou, was hit by an hourly rainfall of 201.9 mm at 1600–1700 Beijing Time (BJT, hereafter), which caused severe urban flooding and economic losses. MCSs were continuously observed over the mid- and northeast-Henan for 3 days and underwent consecutive merging and re-growing processes, playing critical roles in generating the extreme hourly rainfall (Qin et al., 2022; Ran et al., 2021; G. Zhang et al., 2023). The public is deeply concerned about whether this extreme rainfall is related to climate change and worries that such disaster is getting more frequent under global warming. Several studies have investigated the possibility that anthropogenic impacts, such as urbanization, warmer and wetter climate, and more favorable dynamic conditions, can enhance this extreme rainfall event by comparing the current state to the no-anthropogenic state (S. H. Huang et al., 2022; Luo et al., 2023; Qin et al., 2022; Wang et al., 2022). It remains unclear whether human-induced global warming has regulated the characteristics of MCSs and then intensified the localized heavy rainfall in this extreme event.

Focusing on this long-lived MCS in the extreme rainfall event has several benefits when studying the responses of MCS to global warming, including the opportunity to investigate the varying responses at different stages of MCS. Furthermore, adequate moisture condition was provided consistently by water vapor transports from Typhoon In-Fa throughout the 3-day event (Ran et al., 2021; L. Yin et al., 2023). With a constantly sufficient moist supply, this long-lasting MCS is an excellent sample for evaluating the responses of MCSs to global warming. Overall, this study aims to clarify how the MCS in a record-breaking rainfall event responds to global warming, focusing on: (a) How do the characteristics of the MCS, such as strength, area, and structures, change in a warmer climate? (b) Do the responses of the MCS to global warming vary throughout the life cycle of this long-lived MCS?

To estimate the effects of global warming on MCS, a pseudo-global warming (PGW) approach has been adopted in this study. The PGW approach is commonly adopted in studies that quantify the effect of human-induced warming in regional rainfall systems by perturbing the thermodynamic and dynamic component in regional numeric model (Brogli et al., 2023; Kröner et al., 2017; Prein et al., 2017; K. L. Rasmussen et al., 2020; Trapp & Hoogewind, 2016; Wang et al., 2022). Some of these studies perturb both thermodynamic and dynamic fields mimicking the conditions under a warmer climate (Brogli et al., 2023; Liu et al., 2017; Trapp & Hoogewind, 2016). However, another group of studies only perturb the thermodynamic variables (i.e., temperature and moisture) (e.g., Kröner et al., 2017; Prein et al., 2021; Wang et al., 2022), since the thermodynamic responses of warming are much more robust than the dynamic responses, such as the circulation changes. In this study, we focus solely on the thermodynamic effects of warming on MCSs. The PGW approach is implemented in a

10.1029/2023JD039473

regional weather model that reproduces the rainfall process in the Henan extreme rainfall event accurately. We describe the experimental setup and the MCS tracking algorithm in Section 2. The results of MCS rainfall and structure changes under global warming are presented in Section 3. Section 4 presents the varying responses of the MCS during its developing and mature phases. Conclusions and discussion are in Section 5.

2. Model, Data, and Methods

2.1. Numerical Model and Experimental Design

In this study, we employ the Weather Research and Forecasting (WRF, version 4.2.2) model (Powers et al., 2017), which is a fully compressible and non-hydrostatic model. The WRF model is configured with a series of frequently-used physics schemes. The horizontal resolution of our simulations is 4 km, which is within the gray zone of cumulus parameterization. Following a previous study (J. Yin et al., 2022), we adopt the Kain-Frische cumulus parameterization (Sittichai et al., 2016) to better reproduce extreme short-tern rainfall intensity during the selected event. The Purdue Lin cloud microphysics scheme is used to represent detailed microphysics process in the convection (S. H. Chen & Sun, 2002). The Purdue Lin scheme includes all hydrometer including graupel. This scheme is widely used for better reproduce the MCS characteristics during convection and heavy rainfall, and cost less calculation resources than other schemes (Baki et al., 2021; Shi et al., 2021). Besides, we use the Yonsei University planetary boundary layer scheme (Hong et al., 2006), the Monin-Obukhov surface layer scheme, the Noah land-surface model, and the single-layer urban canopy model, the Rapid Radiative Transfer Model for General Circulation Models longwave and shortwave radiation transport scheme (Iacono et al., 2008).

A series of numerical experiments with a 4 km horizontal resolution and 40 vertical sigma level (top at 50 hPa) is conducted to simulate the record-breaking July 2021 Henan extreme rainfall event. There is only one layer of domain with 350 × 300 grids in the west-to-east and south-to-north directions, covering most regions of central-eastern China. Model simulations start at 0800 Beijing Time (BJT) on 18 July 2021, and run for 96 hr. The first 24 hr are treated as the model spin-up times, so this work focuses on the last 72 hr, which covers the heavy rainfall periods. Neither assimilation nor nudging is applied in the simulations.

To estimate the responses of MCS to warming, we adopt the PGW approach to simulate the extreme rainfall events in the real world (RW) and no anthropogenic warming world (NAWW). In each experiment, we run WRF simulations for 100 times, using a stochastic kinetic-energy backscatter scheme (Berner et al., 2011; Shutts, 2005) to generate 100 ensemble members. This large-ensemble approach can provide more robust and reliable estimations of the global-warming effect. For the RW simulation, we use six-hourly reanalysis data from the fifth-generation global reanalysis of the European Centre for Medium-Range Weather Forecasts (ERA5) to derive initial and lateral boundary conditions (Hersbach et al., 2020). The ERA5 reanalysis data include three-dimensional atmospheric, land, and oceanic variables with a 0.25° horizontal resolution. We then update the sea surface temperature field using NOAA's Daily Optimum Interpolation Sea Surface Temperature data set (Reynolds et al., 2002).

The initial and boundary conditions in the NAWW are the same as in the RW experiment, except for the air temperature, specific humidity, and sea surface temperature. Temperature variables are perturbed by removing the anthropogenic warming signals, which are derived from a 16-model ensemble mean of the Coupled Model Intercomparison Project Phase 6 (CMIP6, Eyring et al., 2016). This warming signal is estimated by the temperature difference between the all-forcings experiments (ALL) and nature-forcing-only (NAT) experiments for the period 2011–2020 (the ALL experiment is up to 2014, so the rest 6 years are extended by the SSP2-4.5 experiments). We then re-compute the air specific humidity to keep the relative humidity in consist with the RW. The concentrations of well-mixed greenhouse gases in NAWW are also adjusted to the pre-industrial level, following the forcings in the CMIP6 (Hoesly et al., 2018). By the design of this experiment, temperature, and humidity in the NAWW are those in RW minus the anthropogenic warming and wetting, while other circulation variables remain unchanged. Only modifying the thermodynamic variables can lead to dynamic imbalance in the initial conditions (e.g., Liu et al., 2017; Sørland et al., 2016); however, the dynamic imbalance is quickly smoothed out by dynamic adjustments within first few hours during the spin-up stage. The effects of the adjustment on geopotential and wind are relatively weak. As suggested by previous studies (Kröner et al., 2017; Prein et al., 2017; Wang et al., 2022), the dynamic imbalance due to only using thermodynamic perturbation may be negligible (detailed discussion is in Section 5). The responses of MCSs are the results of the thermodynamic process due to anthropogenic warming, and possible large-scale weather pattern changes are not considered in this experiment (Kröner et al., 2017).

2.2. Model Validity

The 3-day average surface air temperature is about 0.3–1.2°C warmer in RW than NAWW, leading to approximately 5%–8% more precipitable water (Figures 1a and 1b). For the domain average, the ensemble-mean temperature increases by 0.8°C, which is corresponding to the warming signal at the lowest level in CMIP6 (Figure 1c). Consistently, when the MCS has not cooled the environment at 0800 BJT 19 July, the temperature difference is 0.8°C. So, this 0.8°C forcing is used to discuss whether the response of rainfall can exceed the CC rate. The response of rainfall is dependent to the vertical structure of warming signal added to the model (J. Chen et al., 2020; Muller, 2013; Singleton & Toumi, 2013). In our experiment, the warming in low-level is slightly lower than the mid-to-upper troposphere due to the greenhouse gases emission. When comparing the RW simulation to rainfall observations from Integrated Multi-satellitE Retrievals for GPM (IMERG, Huffman et al., 2014), the 3-day accumulated rainfall shows that the WRF model accurately captures the key feature of the extreme rainfall event (Figures 1d and 1e). Both observed and simulated rain bands are located along Taihang Mountain and the maximum rainfall locates at the entrance of a trumpet-shaped valley in mid-Henan. It is worth noting that the rainfall intensity in the WRF simulation is stronger than the IMERG observation data, possibly because the IMERG underestimates some rainfall processes in the extreme event (Gan et al., 2023). Here, the simulated rainfall is more consistent with the gauge-radar-satellite merged hourly rainfall product by the China Meteorological Administration (see Figures 1a and 1b in Wang et al. (2022)), providing further evidence of the experiment's validity.

2.3. MCS Tracking Algorithm

We identify and track the MCSs using the Method for Object-based Diagnostic Evaluation (MODE) and merging in the time dimension (MODE Time Domain, MTD, Davis et al., 2006a, 2006b). This algorithm comprises four steps. First, the hourly rainfall output from the WRF model undergoes horizontal smoothing using a 32 km × 32 km (8 grids width) moving window. Second, the smoothed field is masked by a threshold of 5 mm/hr to identify heavy rainfall areas. Third, the masked fields of each hour are stacked together to identify a continuous rainfall system that is three-dimensionally connected. Lastly, any rainfall system with more than 2000 temporally contiguous grids is marked as an MCS.

During the developing phase, the heavy rainfall areas are widely distributed over the Henan province (Figure 1f, using the first ensemble of RW as an example). As the system matures, these scattered MCS regions merge into a rain cluster and form a large MCS (Figure 1g). In any RW and NAWW ensemble, we can identify a three-day-lasting MCS (hereafter referred to as main MCS, solid lines in Figures 1f and 1g) that accounted for over 90% of the total accumulated rainfall in the domain. The other MCSs (dashed lines in Figures 1f and 1g) are much smaller and do not merge into the main MCS. Hereafter, we focus on the main MCS only.

3. Response of MCS to Warming

We examined the characteristics of the main MCS in each ensemble member in RW and NAWW experiments and compare them using 100-member ensemble means (Figure 2). The simulations demonstrated a clear evolution of the MCS life cycle. From 0800 to 2200 BJT 19 July, the rainfall volume, intensity, and MCS area increase swiftly (Figures 2a–2c), representing the MCS developing phase (light blue boxes in Figure 2). The area and rainfall volume reached their peaks at 0600 BJT 21 July. The MCS average intensity shows three peaks at 0800 BJT 20 July 0800 BJT, and 2300 BJT 21 July, respectively (Figures 2a–2c). The maximum hourly rainfall intensity ($P_{\max}$, defined as the max model-grid rainfall in the MCS) is continuously larger than 80 mm/hr since the mature stage of the MCS (Figure 2d). Two peaks are found at 1000 BJT 20 July and 2000 BJT 21 July with $P_{\max}$ even greater than 110 mm/hr in RW with largest difference to NAWW (black marks in Figure 2d).

With the domain-mean 2-m temperature being 0.8°C warmer in RW than in NAWW, the rainfall volume of MCS increases correspondingly by 10.0% (Figure 2a). The MCS area in RW increases by 3.1% and rainfall intensity increases by 6.7% compared to NAWW (Figures 2b and 2c), both of which are contributing factors to the intensification of the rainfall volume. The increase of MCS area is qualitatively consistent with previous studies for extreme precipitation events (e.g., Dai & Nie, 2022; Prein et al., 2017). The increase in rainfall intensification

Journal of Geophysical Research: Atmospheres

10.1029/2023JD039473

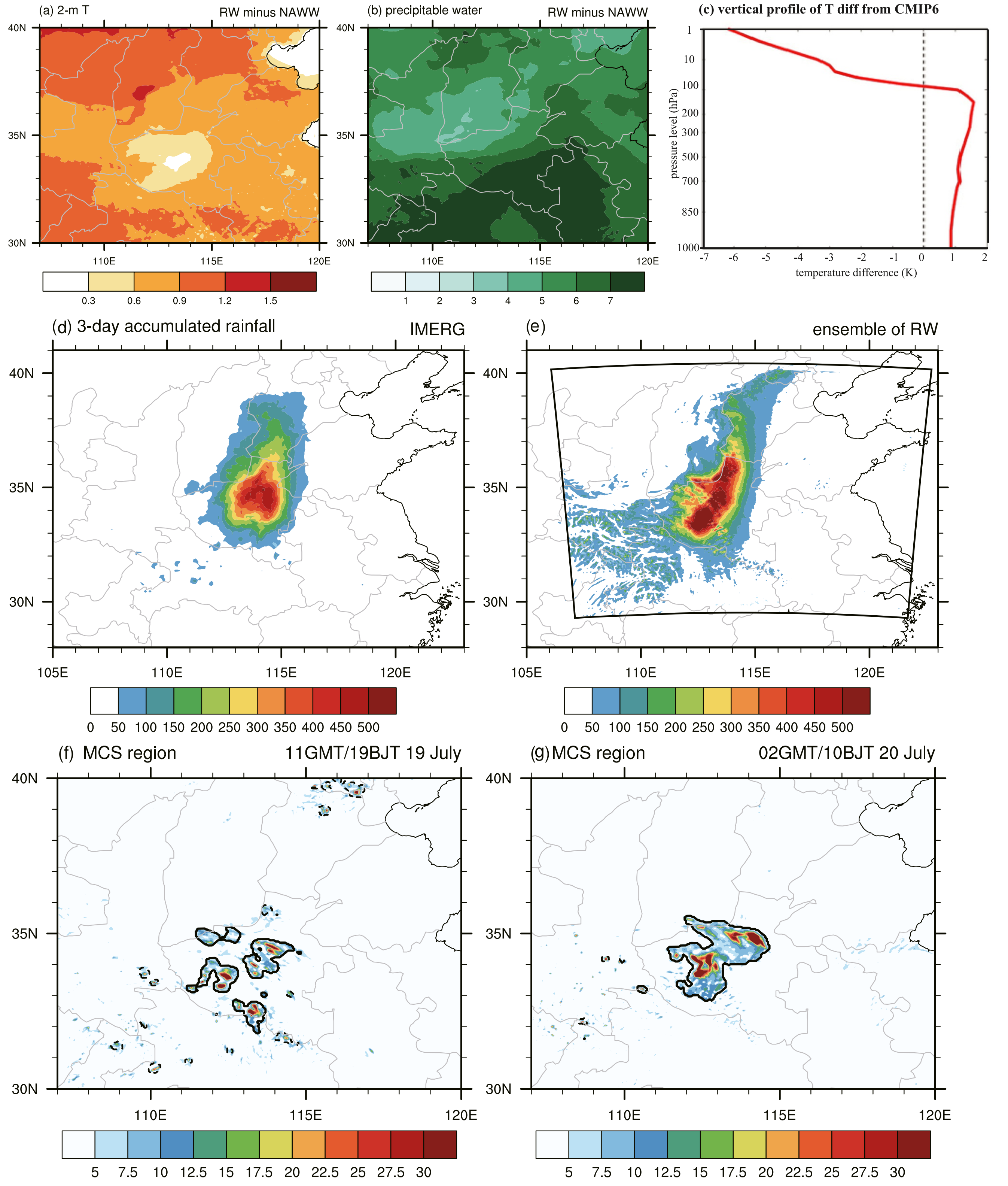

Figure 1.

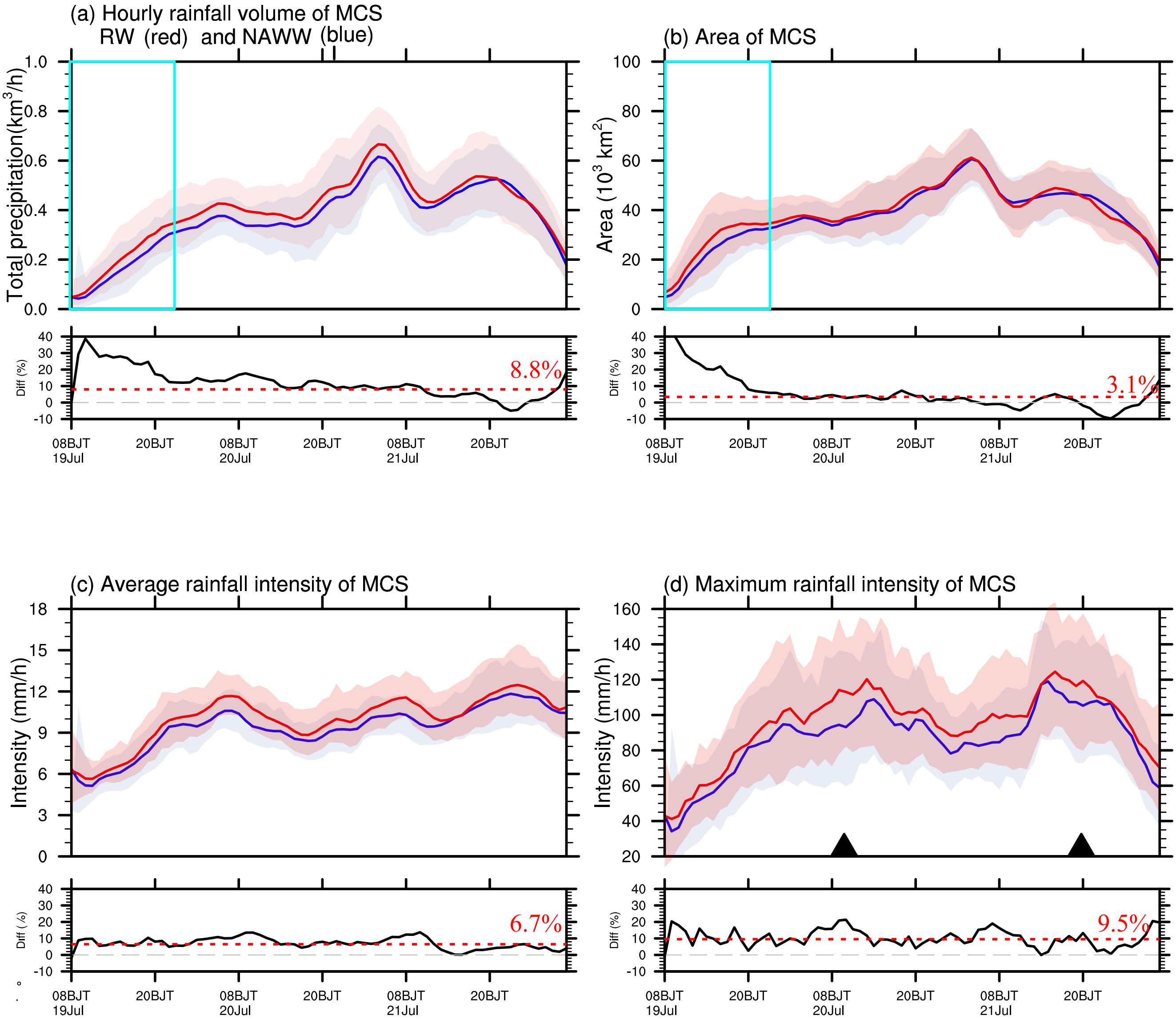

Figure 2. The time series of the main MCS's hourly rainfall volume (a, units: km^3/h), area (b, units: 10^3 km^2), average hourly rainfall intensity (c, units: mm/h), and maximum hourly rainfall intensity (d, P_{max}, units: mm/h) in real world (RW) (red lines) and NAWW (blue lines). Red (blue) shades denote the range of 10–90 percentile of 100 members in RW (NAWW). In the lower panels, the black lines are the fractional differences between RW and NAWW (units: %), the red dashed lines denote the time averages, and the gray dashed lines denote the level of 0% differences. The light blue square shows the period of the developing phase. Two P_{max} peaks are marked by the black triangle.

is estimated at 8.4%/K (calculated based on a 6.7%/0.8 K increase) in MCSs, which is higher than the CC rate of 7%/K.

We also find that the MCS shows varying responses during its developing and mature phases. Specifically, in the developing phase from 0800 to 2200 BJT 19 July (light blue box in Figure 2), the MCS experiences a 20%–40%

Figure 1. Validity of model simulations and mesoscale convective system (MCS) tracking algorithm. (a and b) Spatial distributions of 2-m surface air temperature (a, units:°C) and precipitable water (b, units:%) differences between real world (RW) and no anthropogenic warming world (NAWW) experiments. (c) The vertical profile of atmospheric temperature change in July 2011–2020 over the administrative area of Henan Province (110°–117°E; 31.5°–36.5°N) due to historical anthropogenic forcings estimated from CMIP6 models. (d and e) Three-day accumulated precipitation (0800 BJT 19 July to 0800 BJT 22 July, units: mm) in Integrated Multi-satellitE Retrievals for GPM (IMERG) product (d) and RW experiment (e). The black frame denotes the domain region. (e,f) Hourly precipitation (units: mm/h) at 1900 BJT 19 July (f) and at 1000 BJT 20 July (g). Solid black lines represent the region of the main MCS and dashed black lines denote the smaller MCSs that are ignored in this study. In all figures, the gray lines represent the province boundary of China, and the bold gray lines highlight the Henan Province.

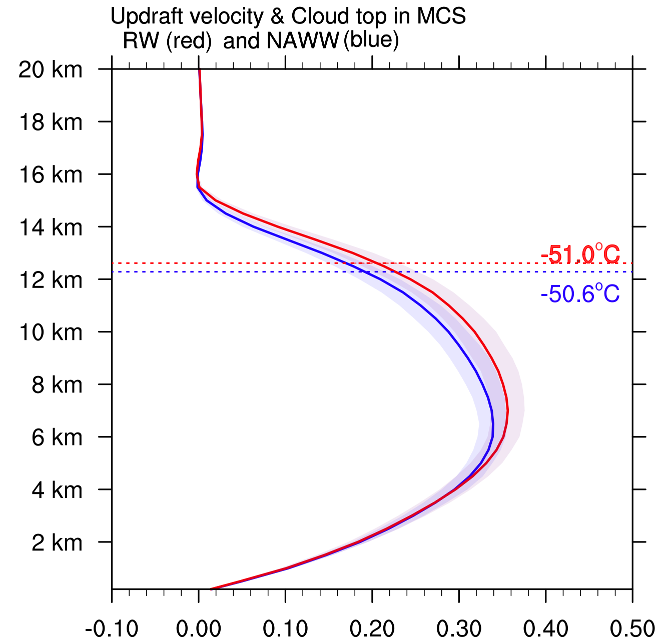

Figure 3. The vertical profile of MCS-mean updraft velocity (m/s) in real world (RW) (red line) and NAWW (blue lines). Red and blue shades denote the range of 10–90 percentile of 100 members in RW and NAWW, respectively. The dashed lines and the temperatures denote the MCS-mean cloud top height and cloud top temperature in RW (red line) and NAWW (blue lines). Cloud top is the highest level where the total hydrometers mixing ratio is larger than 0.01 g/kg.

more rainfall volume due to warming. However, during its mature phase between 2200 BJT 19 July and 2000 BJT 21 July, the MCS only shows a 10% increase in rainfall volume. Furthermore, the developing MCS area is 10%–50% larger in RW compared to NAWW, while during the mature phase, the MCS areas are similar (Figure 2b). As a contrast, the averaged increase of rainfall intensity is relatively constant (Figure 2c) throughout the developing and mature phases. After 2000 BJT on 21 July, the fading of MCS in RW and NAWW is on a similar path. In summary, the response of MCS to the warming climate is characterized by faster growth during the developing phase and stronger intensity throughout the whole MCS life cycle.

Warming may also alter the dynamic structure of MCS in significant ways and eventually affect the rainfall response. In RW, the 3-day mean vertical velocity in the MCS region is about 0.02–0.04 m/s stronger than in the NAWW at the height from 4 to 14 km, indicating about 10% stronger in the upward wind speed (Figure 3). A stronger updraft is favorable for transporting moisture to the upper atmosphere and leads to stronger latent heat release. As a result, the cloud top of MCS is raised by 400 m and the cloud top temperature is cooled by 0.4°C in RW, indicating the MCS extends vertically in a warmer climate.

Deeper MCSs in a warming climate can lead to corresponding responses in hydrometers. The wetter atmosphere is reflected in the increasing mixing ratio of water vapor in the troposphere (Figure 4a). Moreover, different hydrometers exhibit contrasting responses near the freezing levels, within the cloud, and near the cloud top. For liquid condensate, the mixing ratios of cloud and rain increase below the freezing level by 0.03~0.1 g/kg (Figure 4b). Previous studies have suggested that raindrops can fall faster than snow or ice, so a higher concentration of liquid condensate tends to enhance downdrafts and intensify rainfall (R. Rasmussen et al., 2011; Yuter et al., 2006). Meanwhile, a comparison of the mixing ratio of solid condensate shows that snow and ice reduce by 0.01 g/kg between 6 and 10 km altitude in the RW compared to the NAWW but increase at a similar level between 10 and 16 km (Figure 4c). This implies that, due to warming and rising cloud tops, freezing occurs at a higher altitude. Additionally, the mixing ratio of graupel increases above 5 km height but decreases below it, which could be a result of the raising freezing level (Figure 4d). These changes in atmospheric hydrometers associated with global warming favor the generation of intense rainfall.

Our findings suggest that the MCS total rainfall amount is intensified at a level of 8% by a 0.8°C anthropogenic warming, which is in a super-CC scale. The main MCS covers 3.1% more area and the rainfall intensity inside

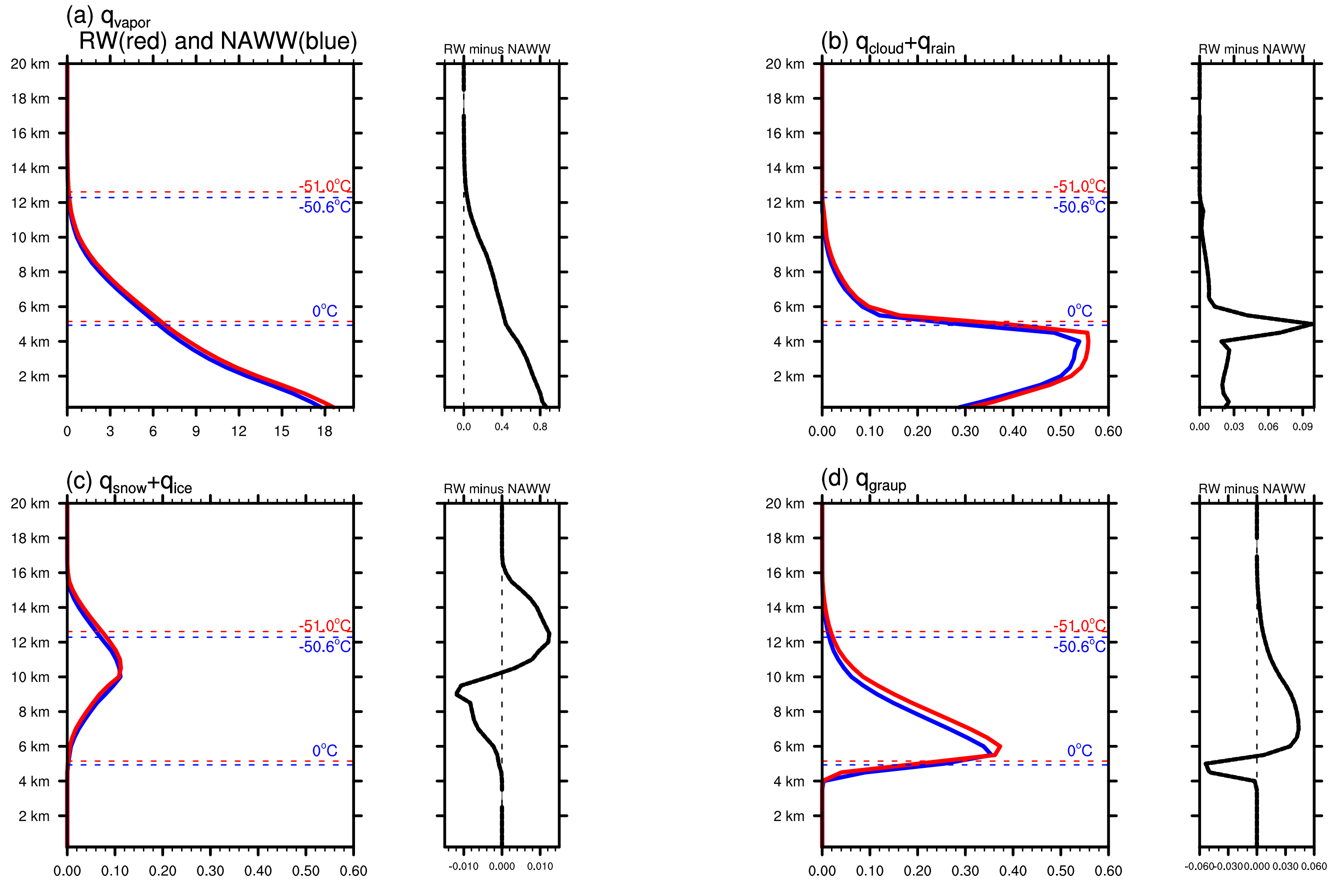

Figure 4. The vertical profile of MCS-mean mixing ratio (g/kg) of water vapor (a, q_{vapor}), liquid condensate (b, $q_{\mathrm{cloud}} + q_{\mathrm{rain}}$), solid condensate (c, $q_{\mathrm{snow}} + q_{\mathrm{ice}}$), and graupel (d, q_{graupel}) in real world (RW) (red line) and NAWW (blue lines). Upper dashed lines denote the cloud top height and the cloud top temperature is shown in RW (red line) and NAWW (blue lines), while the lower dashed lines denote the freezing level. In the right panels, the black lines are the differences between RW and NAWW, and the values that do not pass the 10% level of statistical significance are marked by thin black lines.

MCS is also 6.7% stronger. The updraft is enhanced by ∼10% so the MCS become deeper in a warmer climate. Changes in hydrometer components in response to warming also provide favorable microphysics conditions for generating extreme precipitation. Besides, we also find varying responses of MCS area and intensity in developing and mature phases due to global warming, which will be studied in the next section.

4. Varying Responses in Developing and Mature MCS

As previously stated, the MCS grows much faster in RW than in NAWW. For the multi-member ensemble in RW, the area of MCS increases swiftly between 0800 and 2200 BJT 19 July, but MCS in NAWW grows for six more hours until it reaches the same size as in RW (Figure 2b). At 1800 BJT when the areas of MCS have maximum difference, the rainfall region locates in the middle of Henan Province (Figure 5a), where more than half of members identify MCS in RW. The rainfall intensity is 3–5 mm/hr weaker in NAWW than in RW, and the most notable contrast is at the rainfall center and its upstream (southeast) region (Figure 5b). As a result, more members can identify MCS around the rainfall region, and this contrast is even clearer in the rainfall center where 20 more ensembles can identify MCS in RW than NAWW. Note that occurrences of rainfall and MCS increase uniformly and locally with negligible shifts in the rainfall region. This indicates that warmer environments tend to accelerate the growth of existing MCS rather than promote MCS initiation in the upstream direction.

To discuss how the warmer and wetter environment brought by global warming accelerates the MCS growth, we compare the evolutions of Convective Available Potential Energy (CAPE) and Convective Inhibition (CIN) energy averaged over a broader region of the MCS (31°–36°N, 110°−116°E, black square in Figure 5a, grids

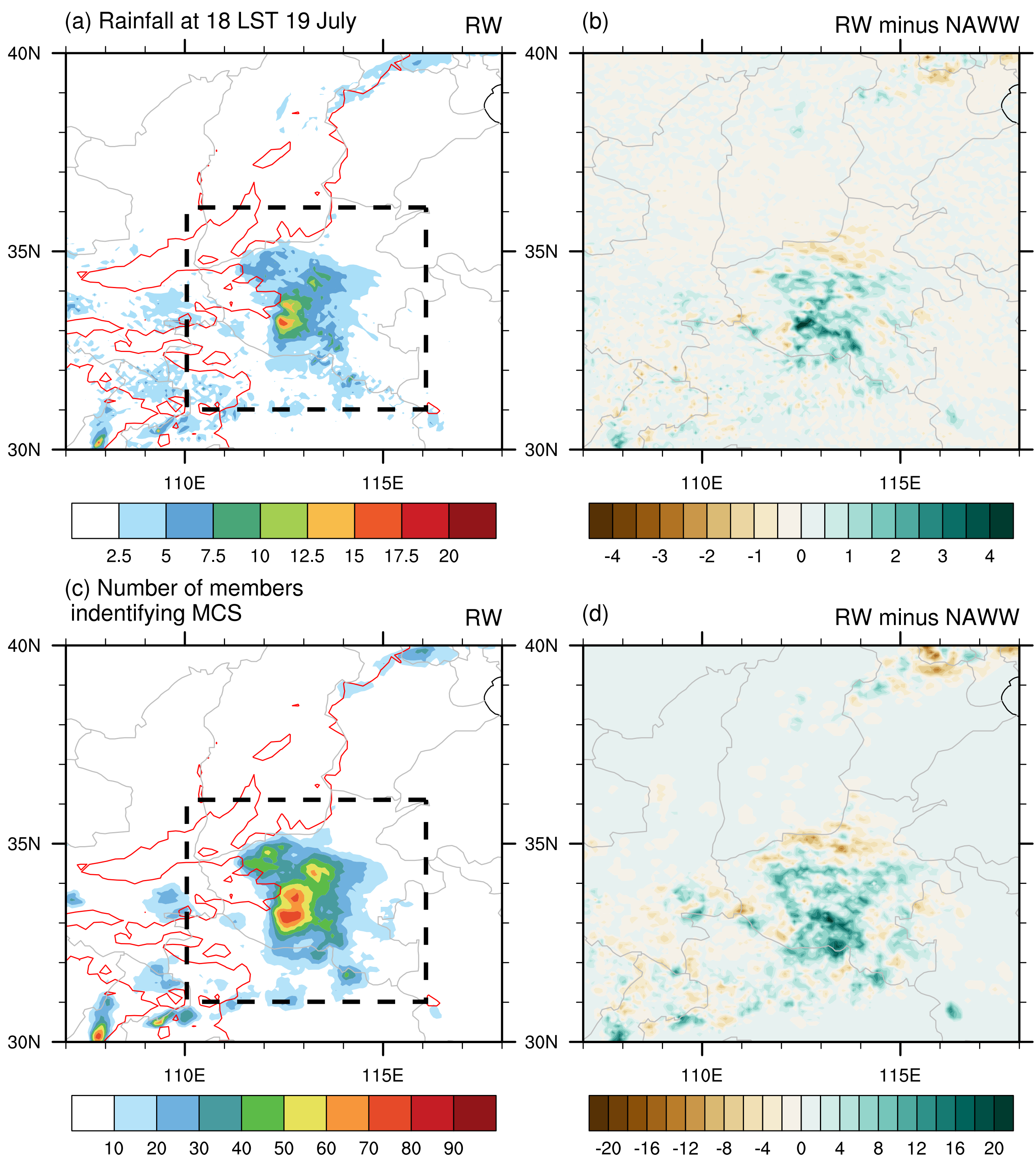

Figure 5. The spatial distribution of rainfall (a, units: mm/h) and numbers of members identifying mesoscale convective system (c, units: member) at 1800 BJT 19 July in real world (RW) and their relative differences between RW and NAWW (b and d). Black dashed boxes denote the region for high-CAPE and low-CIN calculation in Figure 6.

identified as MCS region are excluded). Here, we focus on the covered areas of high-CAPE (grids with CAPE higher than 1,200 J/kg) and low-CIN (grids with CIN lower than 10 J/kg) region. Previous studies suggest that global warming has led to a lower CIN energy, resulting in an expansion of regions with low CIN where

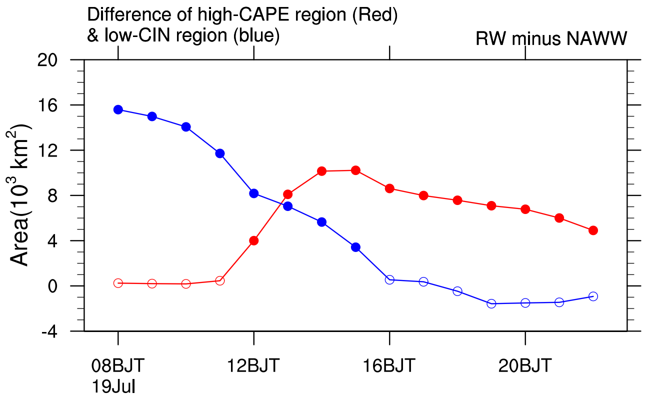

Figure 6. The area difference (real world (RW) minus NAWW) of high-CAPE energy region and low-CIN energy region (units: 10^3 km^2) between 08 BJT to 22 BJT in 19 July in the environment (within 31°–36°N, 110°–116°E and grids in mesoscale convective system are excluded). The high-Cape region is defined as the region with Convective Available Potential Energy at 1 km above surface greater than 1,200 J/kg and low-CIN region is the region where Convective Inhibition at 1 km above surface is lower than 10 J/kg. Solid dots denote that the differences between the 100-member ensemble in RW and NAWW are statistically significant at the 10% level using a two-tail student *t*-test and empty dots represent insignificant differences.

convection is more easily initiated (J. Chen et al., 2020). Consistent with this mechanism, there is about 11,500–15,600 km^2 increase of low CIN region in RW than in NAWW from 0800 to 1100 BJT (Figure 6). Meantime, the high CAPE region is barely found in RW and NAWW as the warm and moist low-level flow has not yet arrived. Since the moisture inflow is enhanced at 1200 BJT, the high CAPE area contrast increases rapidly due to the warmer and wetter atmosphere in RW. Since then, high- CAPE region covers about 6,400–10,200 km^2 more area in RW than in NAWW until 2000 BJT, resulting in a more rapid MCS development in RW. However, during the same period, the low CIN area reduces much faster in RW due to the faster MCS growth (Emanuel et al., 1994; Parker, 2002). After the MCS stops growing in RW at 1800 BJT, the low CIN region in NAWW covers an even larger area than in RW, which is favorable for MCS to keep on growing in NAWW and catch up with the MCS size in RW. Overall, the higher CAPE energy in RW leads to the rapid growth of MCS, but it also narrows down the low CIN region so the MCS growth stagnates earlier in RW than in NAWW.

The intensification of extreme short-term rainfall due to warming has been widely discussed (Miao et al., 2016; Westra et al., 2014). In this study, we are also concerned about the responses of extreme MCS rainfall intensity and location to the warming climate. Two P_{max} peaks are found at 1000 BJT 20 July and 2000 BJT 21 July (black triangle mark in Figure 2d), when the ensemble-mean P_{max} can be greater than 110 mm/hr in RW with largest response. At these peak times, the intensification of P_{max} yields a response rate of 26.5%/K and 17.5%/K, respectively, which significantly surpasses a double or even triple CC rate (Figure 2d).

The MCS shows quite different structures during the two rainfall peak periods, and this may lead to different responses of rainfall centers. During the first P_{max} peak (1000 BJT 20), the rain band is clustered in the mid-Henan Province, where the south-easterly flow from Typhoon In-Fa curves and converges (Figures 7a and 7b). The terrains provide a trumpet-shaped valley, making the MCS rainfall confined in this region. The rainfall intensifies uniformly over the entry of the valley in response to warming, and the rainfall centers are strengthened by more than 20% in RW than NAWW (Figure 7c). The rain band position barely shifts due to warming, and the multi-ensemble average of P_{max} holds its position (Figure 7c).

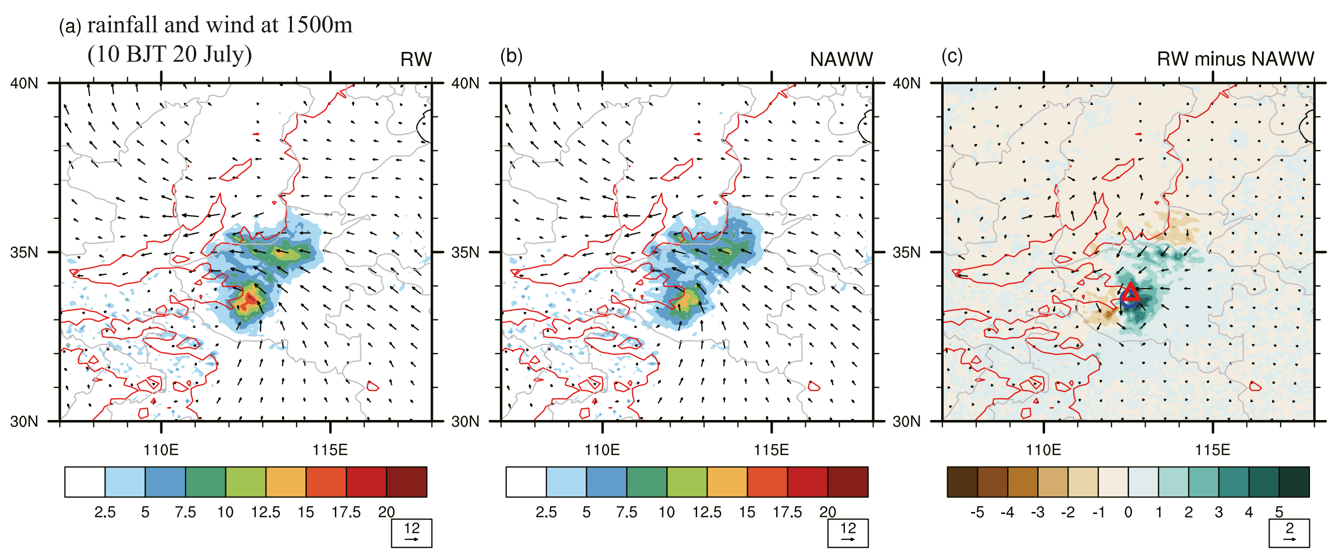

Figure 7. The spatial distribution of rainfall (mm/h) and wind at 1500 altitude (m/s) at 1000 BJT 20 July in real world (RW) (a), NAWW (b) and difference (c, RW minus NAWW). Blue (RW) and red (NAWW) marks are the 100-member ensemble average of P_{max} location.

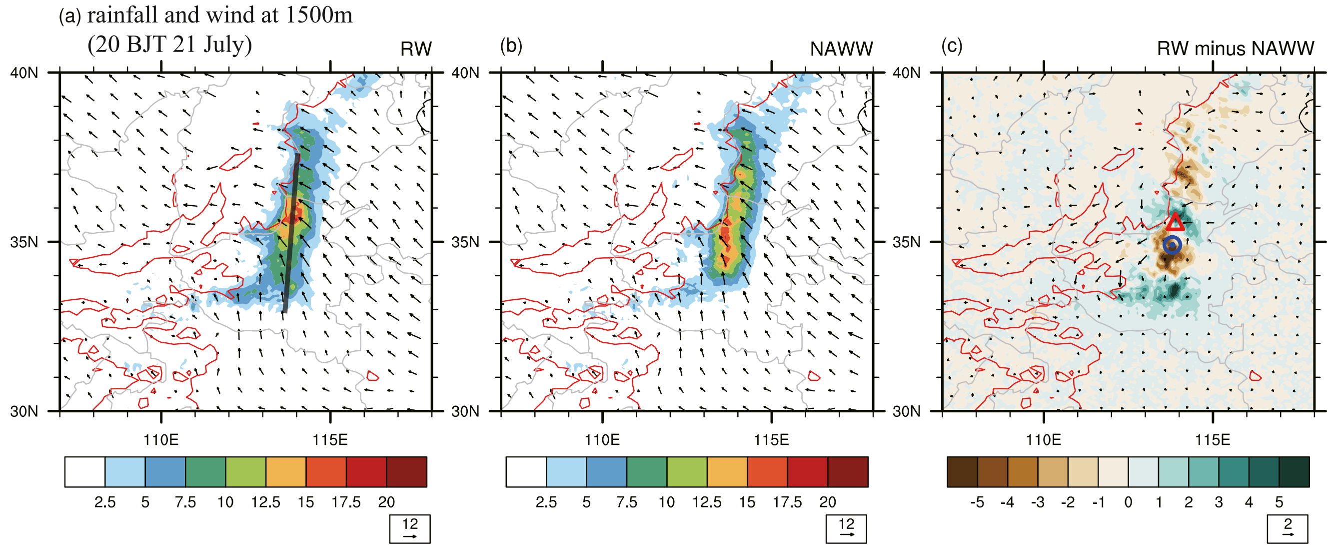

Figure 8. Same as Figure 7, but at 2000 BJT 21 July. Black line denotes the region of vertical section for Figure 9.

During the second peak (2000 BJT 21), the rain band is located east of Taihang Mountain, along the ridges (Figures 8a and 8b). The convergence of southerly and easterly flows extends along the slope, but it is much weaker and less concentrative than in the first peak. As a result, this line-shaped rainfall shows more complicated responses to global warming. When comparing the rainfall in RW to NAWW, positive and negative anomalies appear alternatively along the ridge from south to north (Figure 8c). The anomalies indicate a shift of rainfall toward the upstream (south) direction, suggesting that the heavy rainfall is easier to be triggered in the southerly moist flow. This is further supported by the finding that the ensemble-mean location of P_{max} shifts 80 km in RW than in NAWW (Figure 8c). Note that as the large-scale circulation outside the MCS region shows little difference (Figure 8c), the result of precipitation shift might be more associated with global warming.

We have generated a south-north vertical section across the rainband region during the second peak (black line in Figure 8a) to investigate the relationship between the shift of the rainband and P_{max} and global warming (Figure 9). We observed a significant increase in equivalent potential temperature (θ_e) in the RW compared to

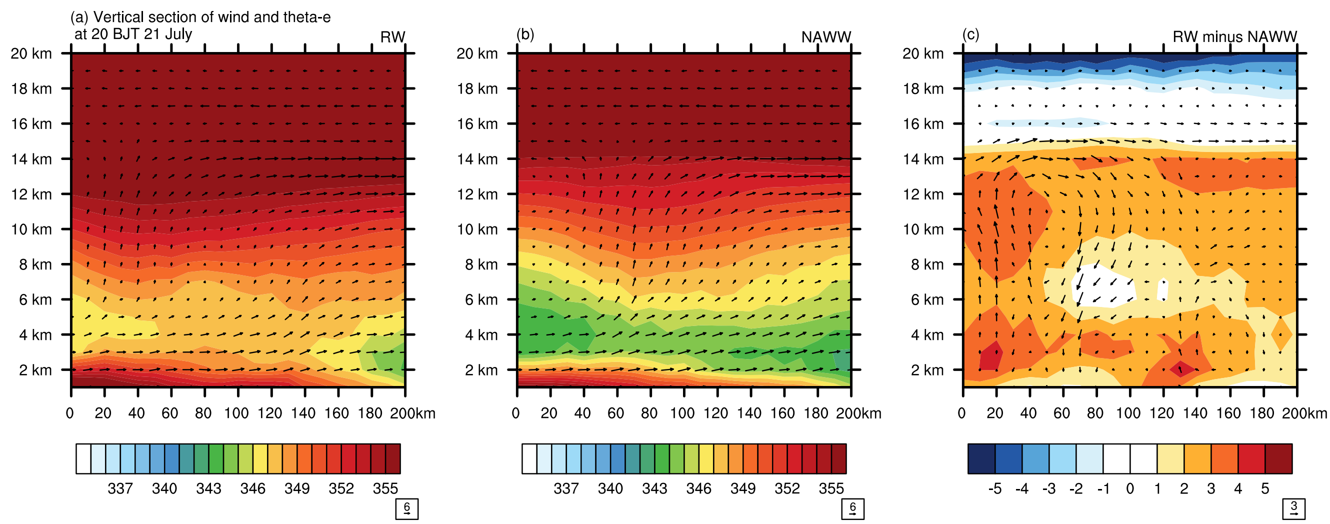

Figure 9. The south-north vertical section of wind (units: m/s, vertical velocity is timed by 10) and Equivalent Potential Temperature (θ_e, units: K) at 2000 BJT 21 July in real world (RW) (a), NAWW (b) and their difference (c, RW minus NAWW). The south-north vertical section starts from the southern edge of rainband in RW and the distance to the edge is shown in X axis (km).

the NAWW, which can be attributed to global warming. Specifically, within a 20 km distance from the southern edge of the rainband, the low-level θ_e in the RW is 3 K higher, resulting in a stronger θ_e gradient (Figure 9c). This gradient is also enhanced at 130 km from the southern edge. As a result, both the vertical velocity over the 20 and 130 km regions from the southern edge experience intensification due to global warming, with anomalous descent occurring approximately 50 km north of the anomalous ascent. The locations of these anomalous ascents align with the positive rainfall strength anomaly depicted in Figure 8c. These findings suggest that global warming may amplify the θ_e gradient along the mountain edge, leading to a shift in strong upward motion and the rainband.

Therefore, when the MCS is confined within the valley, warming leads to little shift of rainfall center position. However, when the rain band is along the ridge and moisture convergence comes from upslope flow, the precipitation region and $P_{\max}$ location show a shift, which might be associated with global warming. In the first case, $P_{\max}$ shows a strong increase, while in the second case, the position shift result in a weaker increase of $P_{\max}$. These findings highlight that the response of MCS rainfall to global warming can be complex and regionally specific, depending on the cooperation of moist flow and terrain.

5. Conclusions and Discussion

Based on a series of large-ensemble numerical experiments, this study examines the impact of global warming on the MCS strength, size, and structures during the record-breaking rainfall event in July 2021 over the Henan Province, China. Our results show that the total rainfall volume of the extreme three-day-lasting MCS increases by 10.0%. Both the expanded MCS area and intensified rainfall intensity contribute to the increased rainfall volume, though their responses vary in different stages of the MCS. The results are summarized below.

1. We track the main MCS that lasts for three days in each of the 100 ensemble members of both experiments. Results show that a 0.8°C warming between the RW and NAWW increases the MCS rainfall volume by 10.0%, which is contributed by a 3.1% larger area and 6.7% of stronger rainfall intensity. A comparison of MCS structure reveals that the MCS becomes stronger and deeper in RW than NAWW, characterized by a higher cloud top and a stronger updraft.
2. During the developing phase, the warmer and wetter southeast inflow brings higher-CAPE energy to the rainfall region, accelerating the MCS growth in RW. And with a rapid MCS growth, the low-CIN region shrinks much faster, causing the growth of MCS in RW to reach stagnation 6 hr earlier compared to NAWW. Thus, the MCS growth process is faster but shortened in response to anthropogenic warming, but the MCS covers a similar area by the end of the developing phase, regardless of the warmer and wetter conditions.
3. Two extreme hourly rainfall peaks have different MCS rain band structures, leading to varying responses of $P_{\max}$. When the MCS concentrates on the entry of the trumpet-shaped valley, the $P_{\max}$ increases by 26.5%/K with negligible position movements. However, when the MCS rain band is along the edge of the Taihang Mountain, the $P_{\max}$ is 17.5%/K stronger but its center shifts southward (upstream direction of moist flow) by 80 km in RW compared to NAWW, indicating strong rainfall might be easier to be triggered in warmer condition. Therefore, the structure of MCS rainbands and the corporation between terrains and moist flows are crucial for the strength and location changes of $P_{\max}$.

There are some limitations in this study that need further effort. Our study and another PGW simulation over North America conducted by Prein et al. (2017) indicate that the increase in rainfall intensity is generally in line with the CC rate. However, the increasing trend of MCS rainfall in the central US (20∼40% per decade; Feng et al., 2016) and hourly extreme rainfall in China (up to three times of CC rate; Miao et al., 2016) are both much larger than our results. This implies that the dynamic processes under global warming, which is not considered in the PGW approach, could further enhance MCSs (e.g., Fitzpatrick et al., 2020; Nie et al., 2020; Song et al., 2022). More research is needed to quantify the relative contributions of dynamic and thermodynamic processes to enhancing MCSs.

In many previous studies utilizing the PGW approach, the global warming signal has been derived by comparing future scenarios with the current climate. This comparison allows for an understanding of how current weather systems may behave in a warmer future. However, the experimental design in this study differs slightly as it compares the current climate (RW) to a cooler climate without human-induced global warming (NAWW). This design is particularly suitable for discussing the contribution of historical global warming since the pre-industrial era to the Henan extreme rainfall event. Although the exclusion of the global warming signal from the current climate and the addition of projected warming signal may result in spatial distribution differences, Wang et al. (2022) suggests that the total rainfall for the same events changes by a comparable amount, regardless of whether the global warming signal is added or removed.

When employing the PGW approach with the WRF regional weather model, our experimental design only perturbed the temperature and moisture fields to simulate the responses of MCS to global warming. The troposphere atmosphere expands vertically due to warmer troposphere, so the lifting of pressure levels should be considered. As the geopotential and wind fields can be automatically adjusted with the WRF model, we did not particularly deal with the dynamic fields. However, some studies suggest that without correspondingly modifying the geopotential and wind fields, dynamic imbalances could occur in the simulation (Brogli et al., 2023; Liu et al., 2017; Sørland et al., 2016). In our investigation, the geopotential over the mountainous region consistently remains 2–3 gpm higher in RW than in NAWW since the first hour after model initiation. This difference aligns with the geopotential perturbation amplitude expected under a 0.8°C warming scenario at 925 hPa, calculated by Equation 11 in Brogli et al. (2023). Notably, the geopotential does not exhibit significant differences in horizontal gradients even near high mountains (figures not shown). Overall, perturbing only the temperature and moisture does not lead to substantial dynamic imbalances in our experiment and subsequent findings. However, whether dynamic imbalance could be more significant in various resolution, greater global warming signal or regional model besides WRF, demands further investigations.

Previous studies usually use long-duration simulations (J. Chen et al., 2020; Fitzpatrick et al., 2020; Prein et al., 2017), so MCSs can occur in varying circulation and topographical conditions. In contrast, our PGW approach only accounts for the effects of thermodynamic environment changes on MCS. While experimental settings differ, our research suggests that the faster growth of MCSs is attributed to the larger CAPE, which shares the mechanism of increased occurrence of MCSs under global warming (Cheng et al., 2022; Fitzpatrick et al., 2020; Takemi et al., 2012). Our findings provide additional insights from a different perspective and complement existing research. The results here may also help understand the responses of MCS to large-scale thermodynamic condition anomalies on inter-annual or decadal timescales.

Data Availability Statement

The fifth-generation global reanalysis of the European Centre for Medium-Range Weather Forecasts (ERA5) used for driving WRF experiments were downloaded from the ECMWF Climate Data Store (Hersbach et al., 2020). The monthly atmospheric temperature data in the Coupled Model Intercomparison Project Phase 6 (CMIP6) used for extracting the warming signal is available at WCRP-ESGF websites (Eyring et al., 2016). The NOAA's Daily Optimum Interpolation Sea Surface Temperature data (OISST) is used to prescribe the SST in numeric experiments (B. Huang et al., 2020), which is obtained from NOAA website. The Integrated Multi-satellitE Retrievals for GPM (IMERG) data used for model avidity and is downloaded from the IMERG website (Huffman et al., 2014). The analyses data are archived at Lin (2023).

Acknowledgments
This research was supported by the National Key R&D Program of China Grant 2022YFC3003902 and the National Natural Science Foundation of China (Grant 42075146).

References

Baki, H., Chinta, S., Balaji, C., & Srinivasan, B. (2021). A sensitivity study of WRF model microphysics and cumulus parameterization schemes for the simulation of tropical cyclones using GPM radar data. *Journal of Earth System Science*, *130*(4), 190. https://doi.org/10.1007/s12040-021-01682-3

Berner, J., Ha, S., Hacker, J. P., Fournier, A., & Snyder, C. (2011). Model uncertainty in a mesoscale ensemble prediction system: Stochastic versus multiphysics representations. *Monthly Weather Review*, *139*(6), 1972–1995. https://doi.org/10.1175/2010MWR3595.1

Brogli, R., Heim, C., Mensch, J., Sorland, S. L., & Schar, C. (2023). The pseudo-global-warming (PGW) approach: Methodology, software package PGW4ERA5 v1.1, validation, and sensitivity analyses. *Geoscientific Model Development*, *16*(3), 907–926. https://doi.org/10.5194/gmd-16-907-2023

Chen, J., Dai, A., Zhang, Y., & Rasmussen, K. L. (2020). Changes in convective available potential energy and convective inhibition under global warming. *Journal of Climate*, *33*(6), 2025–2050. https://doi.org/10.1175/JCLI-D-19-0461.1

Chen, S. H., & Sun, W. Y. (2002). A one-dimensional time dependent cloud model. *Journal of the Mathematical Society of Japan*, *80*(1), 99–118. https://doi.org/10.2151/jmsj.80.99

Cheng, T. F., Dong, Q., Dai, L., & Lu, M. (2022). A dual regime of mesoscale convective systems in the East Asian monsoon annual cycle. *Journal of Geophysical Research: Atmospheres*, *127*(13), 1–21. https://doi.org/10.1029/2022JD036523

Dai, P., & Nie, J. (2022). Robust expansion of extreme midlatitude storms under global warming. *Geophysical Research Letters*, *49*(10), e2022GL099007. https://doi.org/10.1029/2022GL099007

Davis, C. A., Brown, B., & Bullock, R. (2006a). Object-based verification of precipitation forecasts. Part I: Application to convective rain systems. *Monthly Weather Review*, *134*(7), 1785–1795. https://doi.org/10.1175/MWR3146.1

Davis, C. A., Brown, B., & Bullock, R. (2006b). Object-based verification of precipitation forecasts. Part II: Application to Convective Rain Systems. *Monthly Weather Review*, *134*(7), 1785–1795. https://doi.org/10.1175/MWR3146.1

Dougherty, E. M., Prein, A. F., Gutmann, E. D., & Newman, A. J. (2023). Future simulated changes in Central U.S. mesoscale convective system rainfall caused by changes in convective and stratiform structure. *Journal of Geophysical Research: Atmospheres*, *128*(4), e2022JD037537. https://doi.org/10.1029/2022JD037537

Emanuel, K. A., David Neelin, J., & Bretherton, C. S. (1994). On large-scale circulations in convecting atmospheres. *Quarterly Journal of the Royal Meteorological Society*, *120*(519), 1111–1143. https://doi.org/10.1002/qj.49712051902

Eyring, V., Bony, S., Meehl, G. A., Senior, C. A., Stevens, B., Stouffer, R. J., & Taylor, K. E. (2016). Overview of the Coupled Model Intercomparison Project Phase 6 (CMIP6) experimental design and organization [Dataset]. *Geoscientific Model Development*, *9*(5), 1937–1958. https://doi.org/10.5194/gmd-9-1937-2016

Feng, Z., Leung, L. R., Hagos, S., Houze, R. A., Burleyson, C. D., & Balaguru, K. (2016). More frequent intense and long-lived storms dominate the springtime trend in central US rainfall. *Nature Communications*, *7*(5), 1–8. https://doi.org/10.1038/ncomms13429

Fitzpatrick, R. G. J., Parker, D. J., Marsham, J. H., Rowell, D. P., Guichard, F. M., Taylor, C. M., et al. (2020). What drives the intensification of mesoscale convective systems over the West African Sahel under climate change? *Journal of Climate*, *33*(8), 3151–3172. https://doi.org/10.1175/JCLI-D-19-0380.1

Gan, F., Zhang, Y., Diao, X., Cao, G., Tan, K., Zhong, X., & Gao, Y. (2023). Performance evaluation of IMERG products based on the extremely heavy rainstorm event (2021) once in a thousand years in Henan, China. *Atmospheric Research*, *285*, 106639. https://doi.org/10.1016/j.atmosres.2023.106639

Haerter, J. O., & Berg, P. (2009). Unexpected rise in extreme precipitation caused by a shift in rain type? *Nature Geoscience*, *2*(6), 372–373. https://doi.org/10.1038/ngeo523

Hersbach, H., Bell, B., Berrisford, P., Hirahara, S., Horányi, A., Muñoz-Sabater, J., et al. (2020). The ERA5 global reanalysis [Dataset]. *Quarterly Journal of the Royal Meteorological Society*, *146*(730), 1999–2049. https://doi.org/10.1002/qj.3803

Hoesly, R. M., Smith, S. J., Feng, L., Klimont, Z., Janssens-Maenhout, G., Pitkanen, T., et al. (2018). Historical (1750–2014) anthropogenic emissions of reactive gases and aerosols from the Community Emissions Data System (CEDS). *Geoscientific Model Development*, *11*(1), 369–408. https://doi.org/10.5194/gmd-11-369-2018

Hong, S. Y., Noh, Y., & Dudhia, J. (2006). A new vertical diffusion package with an explicit treatment of entertainment processes. *Monthly Weather Review*, *134*(9), 2318–2341. https://doi.org/10.1175/mwr3199.1

Huang, B., Liu, C., Banzon, V., Freeman, E., Graham, G., Hankins, B., et al. (2020). Improvements of the Daily Optimum Interpolation Sea Surface Temperature (DOISST) Version 2.1 [Dataset]. *Journal of Climate*, *34*(8), 2923–2939. https://doi.org/10.1175/JCLI-D-20-0166.1

Huang, S. H., Wen, Z. P., Chen, X. D., Guo, Y. Y., & Wang, Z. W. (2022). The Henan extreme rainfall in July 2021: Modulation of the northward-shift monsoon trough on the synoptic-scale wave train. *Advances in Climate Change Research*, *13*(6), 819–825. https://doi.org/10.1016/j.accre.2022.11.001

Huffman, G., Bolvin, D., Braithwaite, D., Hsu, K., Joyce, R., & Xie, P. (2014). Integrated Multi-satellitE Retrievals for GPM (IMERG), version 4.4 [Dataset]. *NASA's Precipitation Processing Center*. ftp://arthurhou.pps.eosdis.nasa.gov/gpmdata/

Iacono, M. J., Delamere, J. S., Mlawer, E. J., Shephard, M. W., Clough, S. A., & Collins, W. D. (2008). Radiative forcing by long-lived greenhouse gasses: Calculations with the AER radiative transfer models. *Journal of Geophysical Research*, *113*(D13), 1–8. https://doi.org/10.1029/2008JD009944

IPCC. (2021). In V. Masson-Delmotte, P. Zhai, A. Pirani, S. L. Connors, C. Péan, et al. (Eds.), *Climate Change 2021: The Physical Science Basis. Contribution of Working Group I to the Sixth Assessment Report of the Intergovernmental Panel on Climate Change* (p. 2391). Cambridge University Press.

Kendon, E. J., Roberts, N. M., Fowler, H. J., Roberts, M. J., Chan, S. C., & Senior, C. A. (2014). Heavier summer downpours with climate change revealed by weather forecast resolution model. *Nature Climate Change*, *4*(7), 570–576. https://doi.org/10.1038/nclimate2258

Kröner, N., Kotlarski, S., Fischer, E., Lüthi, D., Zubler, E., & Schär, C. (2017). Separating climate change signals into thermodynamic, lapse-rate and circulation effects: Theory and application to the European summer climate. *Climate Dynamics*, *48*(9–10), 3425–3440. https://doi.org/10.1007/s00382-016-3276-3

Lenderink, G., Mok, H. Y., Lee, T. C., & van Oldenborgh, G. J. (2011). Scaling and trends of hourly precipitation extremes in two different climate zones—Hong Kong and the Netherlands. *Hydrology and Earth System Sciences*, *15*(9), 3033–3041. https://doi.org/10.5194/hess-15-3033-2011

Lenderink, G., & van Meijgaard, E. (2009). Unexpected rise in extreme precipitation caused by a shift in rain type? *Nature Geoscience*, *2*(6), 373. https://doi.org/10.1038/ngeo524

Lin, Z. (2023). scripts and data for JGR submission (Lin_et_al_2023). *Zenodo*. https://doi.org/10.5281/zenodo.8079696

Liu, C., Ikeda, K., Rasmussen, R., Barlage, M., Newman, A. J., Prein, A. F., et al. (2017). Continental-scale convection-permitting modeling of the current and future climate of North America. *Climate Dynamics*, *49*(1–2), 71–95. https://doi.org/10.1007/s00382-016-3327-9

Luo, Y., Zhang, J., Yu, M., Liang, X., Xia, R., Gao, Y., et al. (2023). On the influences of urbanization on the extreme rainfall over Zhengzhou on 20 July 2021: A convection-permitting ensemble modeling study. *Advances in Atmospheric Sciences*, *40*(3), 393–409. https://doi.org/10.1007/s00376-022-2048-8

Miao, C., Sun, Q., Borthwick, A. G. L., & Duan, Q. (2016). Linkage between hourly precipitation events and atmospheric temperature changes over China during the warm season. *Scientific Reports*, *6*(1), 22543. https://doi.org/10.1038/srep22543

Muller, C. (2013). Impact of convective organization on the response of tropical precipitation extremes to warming. *Journal of Climate*, *26*(14), 5028–5043. https://doi.org/10.1175/JCLI-D-12-00655.1

Ng, C. P., Zhang, Q., & Li, W. (2021). Changes in hourly extreme precipitation over Eastern China from 1970 to 2019 dominated by synoptic-scale precipitation. *Geophysical Research Letters*, *48*(5), e2020GL090620. https://doi.org/10.1029/2020GL090620

Nie, J., Dai, P., & Sobel, A. H. (2020). Dry and moist dynamics shape regional patterns of extreme precipitation sensitivity. *Proceedings of the National Academy of Sciences of the United States of America*, *117*(16), 8757–8763. https://doi.org/10.1073/pnas.191358411

Nie, J., Sobel, A. H., Shaevitz, D. A., & Wang, S. (2018). Dynamic amplification of extreme precipitation sensitivity. *Proceedings of the National Academy of Sciences of the United States of America*, *115*(38), 9467–9472. https://doi.org/10.1073/pnas.1800357115

Parker, D. J. (2002). The response of CAPE and CIN to tropospheric thermal variations. *Quarterly Journal of the Royal Meteorological Society*, *128*(579), 119–130. https://doi.org/10.1256/00359000260498815

Powers, J. G., Klemp, J. B., Skamarock, W. C., Davis, C. A., Dudhia, J., Gill, J. J., et al. (2017). The weather research and forecasting model: Overview, system efforts, and future directions. *Bulletin of the American Meteorological Society*, *98*(8), 1717–1737. https://doi.org/10.1175/BAMS-D-15-00308.1

Prein, A. F., Liu, C., Ikeda, K., Trier, S. B., Rasmussen, R. M., Holland, G. J., & Clark, M. P. (2017). Increased rainfall volume from future convective storms in the US. *Nature Climate Change*, *7*(12), 880–884. https://doi.org/10.1038/s41558-017-0007-7

Prein, A. F., Rasmussen, R. M., Wang, D., & Giangrande, S. E. (2021). Sensitivity of organized convective storms to model grid spacing in current and future climates. *Philosophical Transactions of the Royal Society A: Mathematical, Physical & Engineering Sciences*, *379*(2195), 20190546. https://doi.org/10.1098/rsta.2019.0546

Qin, H., Yuan, W., Wang, J., Chen, Y., Dai, P., Sobel, A. H., et al. (2022). Climate change attribution of the 2021 Henan extreme precipitation: Impacts of convective organization. *Science China Earth Sciences*, *65*(10), 1837–1846. https://doi.org/10.1007/s11430-022-9953-0

Ran, L., Li, S., Zhou, Y., Yang, S., Ma, S., Zhou, K., et al. (2021). Observational analysis of the dynamic, thermal, and water vapor characteristics of the "7.20" extreme rainstorm event in Henan Province, 2021. *Chinese Journal of Atmospheric Sciences*, *45*(6), 1366–1383. https://doi.org/10.3878/j.issn.1006-9895.2109.21160

Rasmussen, K. L., Prein, A. F., Rasmussen, R. M., Ikeda, K., & Liu, C. (2020). Changes in the convective population and thermodynamic environments in convection-permitting regional climate simulations over the United States. *Climate Dynamics*, *55*(1–2), 383–408. https://doi.org/10.1007/s00382-017-4000-7

Rasmussen, R., Liu, C., Ikeda, K., Gochis, D., Yates, D., Chen, F., et al. (2011). High-resolution coupled climate runoff simulations of seasonal snowfall over Colorado: A process study of current and warmer climate. *Journal of Climate*, *24*(12), 3015–3048. https://doi.org/10.1175/2010JCLI3985.1

Rehbein, A., & Ambrizzi, T. (2023). Mesoscale convective systems over the Amazon basin in a changing climate under global warming. *Climate Dynamics*, *61*(3–4), 1815–1827. https://doi.org/10.1007/s00382-022-06657-8

Reynolds, R. W., Rayner, N. A., Smith, T. M., Stokes, D. C., & Wang, W. (2002). An improved in situ and satellite SST analysis for climate. *Journal of Climate*, *15*(13), 1609–1625. https://doi.org/10.1175/1520-0442(2002)015<1609:AIISAS>2.0.CO;2

Shi, Y., Wang, H., Shen, X., Zhang, W., Zhang, M., Zhang, X., et al. (2021). Application of Morrison cloud microphysics scheme in GRAPES_Meso model and the sensitivity study on CCN's impacts on cloud radiation. *Atmosphere*, *12*(4), 489. https://doi.org/10.3390/atmos12040489

Shutts, G. (2005). A kinetic energy backscatter algorithm for use in ensemble prediction systems. *Quarterly Journal of the Royal Meteorological Society*, *131*(612), 3079–3102. https://doi.org/10.1256/qj.04.106

Singleton, A., & Toumi, R. (2013). Super-Clausius–Clapeyron scaling of rainfall in a model squall line. *Quarterly Journal of the Royal Meteorological Society*, *139*(671), 334–339. https://doi.org/10.1002/qj.1919

Sittichai, P., Phakawan, R., Patipat, V., & Sulak, S. (2016). Impacts of cumulus convective parameterization schemes on precipitation at grey-zone resolutions: A case study over complex terrain in upper Northern Thailand. *International Journal of Environmental Science and Development*, *7*(5), 359–362. https://doi.org/10.7763/IJESD.2016.V7.800

Song, F., Leung, L. R., Feng, Z., Chen, X., & Yang, Q. (2022). Observed and projected changes of large-scale environments conducive to spring MCS initiation over the US Great Plains. *Geophysical Research Letters*, *49*(15), e2022GL098799. https://doi.org/10.1029/2022GL098799

Sørland, S. L., Sorteberg, A., Liu, C., & Rasmussen, R. (2016). Precipitation response of monsoon low-pressure systems to an idealized uniform temperature increase. *Journal of Geophysical Research: Atmospheres*, *121*(11), 6258–6272. https://doi.org/10.1002/2015JD024658

Takemi, T., Nomura, S., Oku, Y., & Ishikawa, H. (2012). A regional-scale evaluation of changes in environmental stability for summertime afternoon precipitation under global warming from super-high-resolution GCM simulations: A study for the case in the Kanto Plain. *Journal of the Meteorological Society of Japan*, *90*(A), 189–212. https://doi.org/10.2151/jmsj.2012-A10

Trapp, R. J., Diffenbaugh, N. S., & Gluhovsky, A. (2009). Transient response of severe thunderstorm forcing to elevated greenhouse gas concentrations. *Geophysical Research Letters*, *36*(1), L01703. https://doi.org/10.1029/2008GL036203

Trapp, R. J., & Hoogewind, K. A. (2016). The realization of extreme tornadic storm events under future anthropogenic climate change. *Journal of Climate*, *29*(14), 5251–5265. https://doi.org/10.1175/JCLI-D-15-0623.1

Trenberth, K. E., Dai, A., Rasmussen, R. M., & Parsons, D. B. (2003). The changing character of precipitation. *Bulletin of the American Meteorological Society*, *84*(9), 1205–1218. https://doi.org/10.1175/BAMS-84-9-1205

Wang, J., Chen, Y., Nie, J., Yan, Z., Zhai, P., & Feng, J. (2022). On the role of anthropogenic warming and wetting in the July 2021 Henan record-shattering rainfall. *Science Bulletin*, *67*(20), 1–5. https://doi.org/10.1016/j.scib.2022.09.011

Westra, S., Fowler, H. J., Evans, J. P., Alexander, L. V., Berg, P., Johnson, F., et al. (2014). Future changes to the intensity and frequency of short-duration extreme rainfall. *Reviews of Geophysics*, *52*(3), 522–555. https://doi.org/10.1002/2014RG000464

Yin, J., Gu, H., Liang, X., Yu, M., Sun, J., Xie, Y., et al. (2022). A possible dynamic mechanism for rapid production of the extreme hourly rainfall in Zhengzhou City on 20 July 2021. *Journal of Meteorological Research*, *36*(1), 6–25. https://doi.org/10.1007/s13351-022-1166-7

Yin, L., Ping, F., Mao, J., & Jin, S. (2023). Analysis on precipitation efficiency of the "21.7" Henan extremely heavy rainfall event. *Advances in Atmospheric Sciences*, *40*(3), 374–392. https://doi.org/10.1007/s00376-022-2054-x

Yuter, S. E., Kingsmill, D. E., Nance, L. B., & Löffler-Mang, M. (2006). Observations of precipitation size and fall speed characteristics within coexisting rain and wet snow. *Journal of Applied Meteorology and Climatology*, *45*(10), 1450–1464. https://doi.org/10.1175/JAM2406.1

Zhang, G., Mao, J., Hua, W., Wu, X., Sun, R., Yan, Z., et al. (2023). Synergistic effect of the planetary-scale disturbance, typhoon and meso-β-scale convective vortex on the extremely intense rainstorm on 20 July 2021 in Zhengzhou. *Advances in Atmospheric Sciences*, *40*(3), 428–446. https://doi.org/10.1007/s00376-022-2189-9

Zhang, Q. H., Li, R. M., Sun, J. Z., Lu, F., Xu, J., & Zhang, F. (2023). A review of research on the record-breaking precipitation event in Henan Province, China, July 2021. *Advances in Atmospheric Sciences*, *40*(8), 1485–1500. https://doi.org/10.1007/s00376-023-2360-y